

Seasonal and inter-annual turbidity variability in the Río de la Plata from 15 years of MODIS: El Niño dilution effect



A.I. Dogliotti ^{a, *}, K. Ruddick ^b, R. Guerrero ^c

^a Instituto de Astronomía y Física del Espacio (IAFE), Consejo Nacional de Investigaciones Científicas y Técnicas, Universidad de Buenos Aires, Facultad de Ciencias Exactas y Naturales, Buenos Aires, Argentina

^b Royal Belgian Institute of Natural Sciences (RBINS), Operational Directorate Natural Environment, Brussels, Belgium

^c Instituto de Investigación y Desarrollo Pesquero (INIDEP), Argentina

ARTICLE INFO

Article history:

Received 24 April 2016

Received in revised form

3 August 2016

Accepted 15 September 2016

Available online 16 September 2016

Keywords:

Turbidity

MODIS

Río de la Plata

Bermejo

ENSO

ABSTRACT

Spatio-temporal variability of turbidity in the Río de la Plata (RdP) estuary (Argentina) at seasonal and inter-annual timescales is analyzed from 15 years (2000–2014) of MODIS data and explained in terms of river discharges and the El Niño Southern Oscillation (ENSO). Satellite estimates were first validated using in situ turbidity measurements and then the time series of monthly averages were analyzed to assess the seasonal and inter-annual variability of turbidity. A strong seasonal variability was found in the upper and middle estuary with high turbidity from March to May and low turbidity from June to January. It was found that this variability is highly correlated to the seasonal cycle of the water discharge of the Bermejo river with a one-month delay between its peak and turbidity in the upper RdP estuary. On inter-annual time scales the influence of ENSO shows low turbidity amplitudes in the upper and middle estuary during moderate El Niño years, while the opposite pattern is observed in some La Niña years. A dilution effect during El Niño years is observed given that the main tributaries, which provide ~92% of the liquid discharge, show water discharge increases due to excess in rain, while the Bermejo river, which provides ~70% of the solid discharge and only 2% of the liquid discharge to the RdP, does not show this inter-decadal periodicity. In turn, increased turbidities are observed when negative RdP water discharge anomalies occurred, but this is not always related to La Niña events, since these events are not the only predictor for drought in this region.

© 2016 Elsevier Ltd. All rights reserved.

1. Introduction

Rivers carry nutrients, sediments and pollutants into the coastal ocean affecting the biological, geochemical and physical functioning of the coastal environment. Estimates of the global suspended sediment flux to the oceans range between 15 and 20 10^9 tons y^{-1} (Walling and Webb, 1996), 95% of which are provided by rivers and the remaining 5% by glaciers, sea-ice, icebergs, wind, and coastal erosion (Syvitski, 2003). The magnitude of the sediment load transported by rivers has important implications for the functioning of the natural Earth system. For example, sediments affect light penetration into the water column controlling primary production system which in turn controls the higher trophic levels.

Cohesive sediments, which include primarily clay and organic fractions, act as a carrier for contaminant transport in riverine and estuarine systems given their high sorptive capacity for many chemicals. Thus knowledge of sediments distribution are important for a number of applications including the control and mitigation of pollution, understanding of fisheries, evaluation of particulate organic carbon exported by rivers to the sea, biogeochemical modeling, and optimization of dredging operations.

Understanding and monitoring the distribution of sediments coming from rivers and their temporal variability is complex in coastal environments where the distribution and fluxes of suspended sediments are highly variable and vary over a broad spectrum of temporal and spatial scales. This variability renders most traditional field sampling methods inadequate to study sediment dynamics in complex coastal waters (Miller et al., 2003) making satellite sensors the most suitable tools available to map the river influence on the adjacent ocean, especially in the Río de la Plata (RdP) estuary given its large scale ($\sim 3.5 \times 10^4$ km²). Remote sensing

* Corresponding author.

E-mail addresses: adogliotti@iafe.uba.ar (A.I. Dogliotti), kruddick@naturalsciences.be (K. Ruddick), raul.guerrero@inidep.edu.ar (R. Guerrero).

data have been used to describe the spatio-temporal variability of suspended particulate matter (SPM) of different river plumes and to relate it to the main hydro-climatic forcing (e.g. Devlin and Schaffelke, 2009; Falcini et al., 2012; Schroeder et al., 2012; Loisel et al., 2014; Petus et al., 2014; Fabricius et al., 2016). In a previous work, Moreira et al. (2013) characterized the RdP annual mean SPM concentration distribution using 10 years of satellite data (2002–2012), studied its variability on seasonal time scale and identified the physical mechanisms. They found that in the upper and middle estuary the SPM increases in the austral fall (March–May), reached a peak in austral winter (June–August), and decreased to minimum values in austral summer (December–February). For all large scale measurements of SPM, either in situ or satellite, it is necessary to use an optical proxy. Here water turbidity (T), defined by the International Standards Organisation as particulate side-scattering at 860 nm, has been chosen because it is known to be highly correlated to SPM concentration (Boss et al., 2009). T can easily be converted into SPM using a linear conversion factor, but is preserved here as the primary variable because estimation of T from water reflectance is very reliable (Dogliotti et al., 2015) and because the optical parameter T maybe be useful not just as a proxy for SPM but also, in its own right, for studies of underwater light climate for phytoplankton and marine animals.

The objective of the present study is to quantify the variability of turbidity in the RdP on seasonal and inter-annual timescales and explain this variability in terms of the water discharges of the various upstream rivers, which are in turn influenced by inter-decadal events like El Niño Southern Oscillation (ENSO). This is achieved by the analysis of 15 years (2000–2014) of MODerate Resolution Imaging Spectroradiometer (MODIS) data (Aqua and Terra). Satellite estimates are first validated using in situ turbidity measurements and then time series of monthly composites are analyzed to assess the seasonal and inter-annual variability of turbidity and its relation with Oceanic Niño Index (ONI) and the water discharge of RdP tributaries. Regarding the seasonality and spatial distribution, differences and similarities with previous findings, such as the study of Moreira et al. (2013), are analyzed and discussed.

2. Study area

The La Plata basin is the second major hydrographical basin of South America after the Amazon and the fifth largest in the world (UNESCO, 2007). It covers approximately $3170 \times 10^6 \text{ km}^2$ (Tossini, 1959) distributed in five countries (Argentina, Brazil, Bolivia, Uruguay and Paraguay) and drains to the Atlantic Ocean through the Paraná Delta and RdP estuarine system (Fig. 1A). The RdP river currently delivers a water discharge estimated at $\sim 670 \text{ km}^3$ per year (annual mean discharge of $\sim 22,500 \text{ m}^3 \text{ s}^{-1}$), of which about 79% is supplied by the Parana River and the remaining 21% by the Uruguay River. The RdP carries around 160×10^6 metric tons per year of suspended sediment to the Atlantic, 68% of which is contributed by the upper Paraná-Paraguay Basin (Depetris and Griffins, 1968). In particular, the Bermejo River with average sediment concentrations of 8000 g m^{-3} , amongst the highest in the world, discharges ca. 100×10^6 tons yr^{-1} to the Paraguay River (Pedrozo and Bonetto, 1987; Brea and Spalletti, 2010) providing most of the sediment load arriving to RdP as found from erosion rates, and silt- and clay-size mineralogy studies (Depetris and Griffins, 1968; Drago and Amsler, 1988; Sarubbi, 2007).

The RdP estuary has a northwest to southeast oriented funnel shape approximately 320 km long that can be divided in three regions: upper, middle and outer regions (Fig. 1C). The upper estuary includes the Paraná Delta front and extends to the Buenos Aires-Colonia line; it is a very shallow area (between 1 and 4 m depth)

and has a fluvial regime. The middle estuary extends to the Punta Piedras-Montevidéo line. This transition zone has generally fresh waters, but a marine influence can be detected along the northern margin along the Uruguay coast with higher tidal influence and seawater penetration (Boschi, 1988). The outer region extends up to the limit with the ocean, defined by the Punta Rasa-Punta del Este line, and has an estuarine regime with variable salinity ranging from 10 to 25 psu (Guerrero et al., 2010). Shelf marine waters penetrate the estuary along the bottom and freshwater flows seawards on the surface forming a two-layer quasi-permanent salt-wedge structure which can be mixed to varying degrees depending on wind and current intensities (Guerrero et al., 1997). At the near bottom salinity front, the flocculation of suspended matter at the tip of the salt wedge and the resuspension of sediment through tidal current friction at the bottom results in the development of a turbidity front with mean location strongly related to the bottom topography (Framiñan and Brown, 1996). At the southern coast, in the Samborombón Bay, the mean frontal position coincides with the 5 m depth contour, and to the north it follows the Barra del Indio shoal, a shallow bar that runs along a line from Punta Piedras to Montevideo (Fig. 1C). In the RdP, the main forcing that influences water circulation are continental runoff, tides, and winds. The estuary is characterized by a low tidal amplitude ($< 1 \text{ m}$) (Simionato et al., 2004b), a fast reaction to atmospheric forcing due to its shallow water depth (Simionato et al., 2006, 2007, 2010; Meccia et al., 2009), and weak seasonality of river discharge. At longer time scales the precipitation in the southeast of South America is known to be related to the El Niño Southern Oscillation (ENSO) (Ropelewski and Halpert, 1987, 1989; Aceituno, 1988; Diaz et al., 1998). Rainfall anomalies in northeastern Argentina, southeastern Brazil and Uruguay tend to be positive from November of El Niño years to February of the following years and negative from July to December of La Niña years (Ropelewski and Halpert, 1987, 1989). Many studies have examined the association between ENSO and river discharge in the La Plata basin. Studies focusing on the Paraná (Mechoso and Pérez Iribarren, 1992; Depetris et al., 1996; Robertson and Mechoso, 1998; Robertson et al., 2001; Berri et al., 2002; Camilloni and Barros, 2003), Uruguay (Mechoso and Pérez Iribarren, 1992), and Paraná and Uruguay rivers together (García and Mechoso, 2005) showed that the two main fluvial components, i.e. the Paraná and Uruguay rivers, exhibit a strong interannual oscillation which is in phase with El Niño events (Pasquini and Depetris, 2007). Both rivers show flow increases during ENSO warm events (or El Niño) and normal to low water discharges during cold events (or La Niña). In turn, the Bermejo and Pilcomayo rivers, two small tributaries of the Paraguay river, were found not to follow the El Niño-like interannual periodicity (Pasquini and Depetris, 2007), in contrast to the others RdP tributaries. ENSO events affect precipitation in the southeast region of South America, i.e. mainly the headwaters of the Paraná and Uruguay rivers, while the Pilcomayo and Bermejo upper catchments are located to the west, close to the Andes (see Fig. 1A), and thus are not affected.

3. Data and methods

3.1. Satellite data

MODIS-Aqua (MA) and MODIS-Terra (MT) images were obtained from the NASA Ocean Color web site (<http://oceancolor.gsfc.nasa.gov>). Level 1A files covering the RdP region from 2000 to 2014 for Terra and from 2002 to 2014 for Aqua sensors were downloaded. Images were processed using the freely available SeaDAS 7.02 software to obtain remotely sensed reflectance (R_{rs}) using the near- and shortwave-infrared (NIR-SWIR) switching atmospheric correction algorithm (Wang, 2007; Wang and Shi, 2007) and

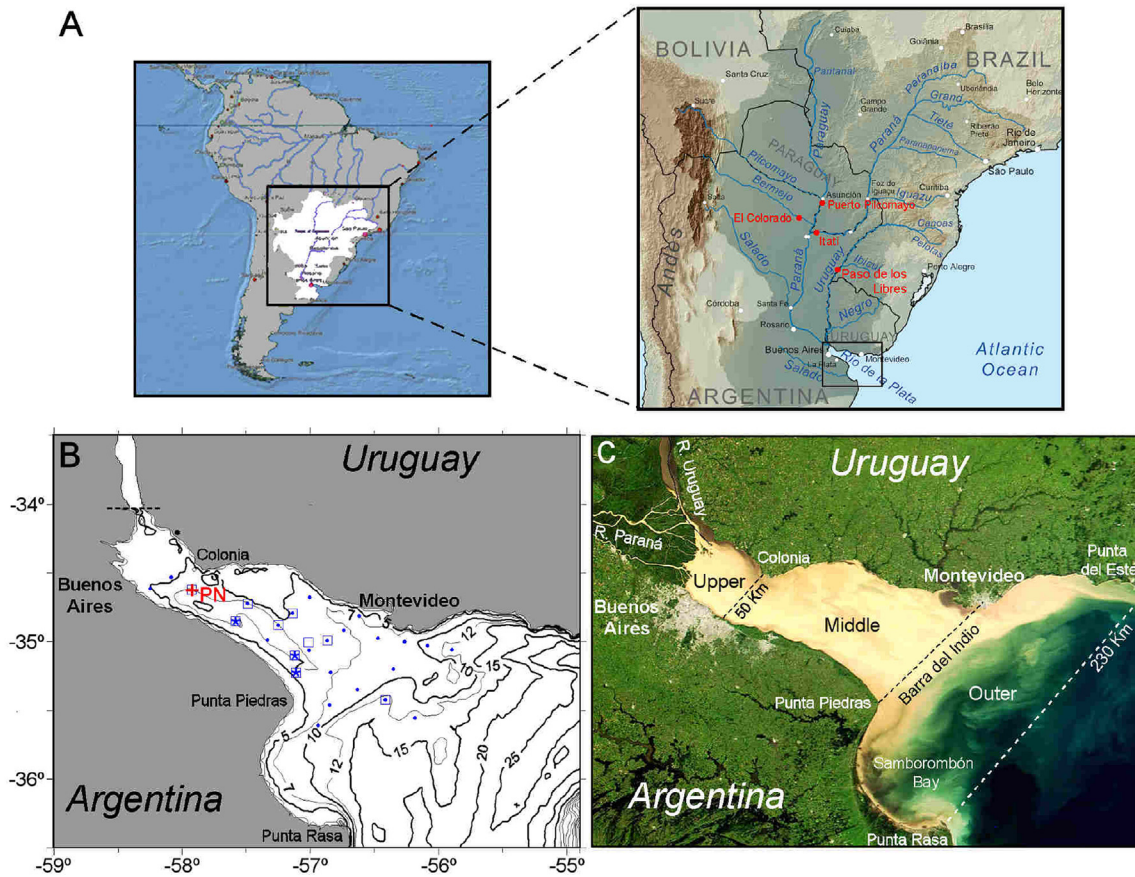


Fig. 1. A) Map of La Plata drainage basin. The rivers, main cities, locations of gauging stations used in this study (in red) and the RdP estuary area (black rectangle) are indicated. B) Bathymetry map with the location of the 26 sampled sites during the oceanographic cruises (all blue dots) and the fixed instrument at Pilote Norden (red cross). The location of MODIS-Aqua (squares) and MODIS-Terra (stars) match-ups are also indicated; C) MODIS quasi-true-color image of the RdP estuary where the Upper, Middle and Outer regions of the estuary are indicated (delimited by the dashed lines). (For interpretation of the references to colour in this figure legend, the reader is referred to the web version of this article.)

masking clouds using the 2130 nm band. The STRAYLIGHT and HILT flags were not used as masks because the highly reflective (turbid) waters and sensor saturation at 667, 748 and 869 nm bands erroneously mask most of the RdP estuary. Turbidity (T) was then estimated using the switching band semi-analytical algorithm described in Dogliotti et al. (2015). Using the approach described in that paper, T can easily be converted into Suspended Particulate Matter (SPM) concentration by using local, linear conversion factors, like $SPM = 0.73 \times T$ in Moreira et al. (2013), and so all conclusions from the present study apply equally to turbidity and SPM.

To analyze the algorithm performance (match-up analysis), field data collected during six oceanographic cruises and from a fixed tower were used (see details below). Satellite-derived T were extracted from cloud-free Level 2 daily images acquired during each cruise and for each sampled site using the median value in a 3×3 pixel box centered at the location of each site if at least 6 out of the 9 pixels were valid pixels according to the standard flags. Homogeneity was tested and a match-up was considered valid if the coefficient of variation (standard deviation to mean ratio) was less than 0.2. Regarding the temporal window between satellite overpass and field measurements, a ± 3 hs window was used for the cruise data, while a ± 5 min temporal window was used for the fixed instrument that collected data every 15 min.

For the time series analysis, MODIS-Aqua (2002–2014) and MODIS-Terra (2000–2014) daily images were mapped to a cylindrical equidistant projection at 0.0833° spatial resolution (~ 1 km) and monthly averaged turbidity maps were obtained. In order to

illustrate the relative annual change in turbidity, the inter-annual turbidity anomaly maps were calculated as the difference between the yearly mean of each complete calendar year and the composite annual mean of all 15 calendar years analyzed.

3.2. Field data

In situ surface turbidity measurements, used to evaluate satellite retrievals, have been collected during oceanographic cruises and from an in-water instrument located in a fixed site in the frame of the FREPLATA Project (Simionato et al., 2011). Six oceanographic campaigns (named IFR-1 to 6) have been performed between November 2009 and December 2010 (Table 1). Near surface water

Table 1

Summary of cruises and fixed site, date of sampling, turbidity range [minimum–maximum], and number of match-ups. The number of cloud-free images are indicated between parentheses.

	# St.	Dates	T Range	Match-ups (images)	
			[FNU]	MODIS-A	MODIS-T
IFR-1	26	23–28 Nov 2009	4–211	0	0
IFR-2	26	17–19 Mar 2010	6–180	0	0
IFR-3	26	23–25 Jun 2010	5–462	5 (2)	1 (1)
IFR-4	26	23–27 Aug 2010	2–110	1 (1)	2 (1)
IFR-5	26	25–28 Oct 2010	2.3–132	4 (1)	1 (1)
IFR-6	24	15–17 Dec 2010	4.5–627	1 (1)	0
P. Norden	15 min.	8 Apr–27 Aug 2010	16–681	24 (63)	26 (46)

samples (2–4 m) were collected in 26 stations (dots in Fig. 1B) using a pump and turbidity measurements were performed on board using a portable HACH 2100P ISO turbidimeter which records values between 0 and 1000 Formazin Nephelometric Units (FNU). High frequency turbidity measurements were also collected at a fixed site named Pilote Norden (PN) located at 34°37.77' S - 57°55.184' W (red cross in Fig. 1B). At this site a NKE SMATCH TT Multiparameter probe with a Seapoint Optical Sensor (wavelength of light source 880 nm), mounted at about 2 m above the river bed, collected turbidity data every 15 min for 5 months (Table 1). The sensor was calibrated with Formazin at the laboratory before deployment.

3.3. River discharge data

A time series of monthly water discharge of the RdP corresponding to the period 1931–2014 was obtained from Borús and Giacosa (2014). These values are not directly measured but estimated from measurements of the three main tributaries, i.e. Uruguay, Paraná de las Palmas and Paraná Guazú, in locations close to their outlet. Monthly mean water discharge of four tributary rivers for the 2000–2014 period were obtained from the Integrated Hydrologic Database provided by the Argentine Subsecretaría de Recursos Hídricos (<http://www.hidricosargentina.gov.ar/>). The water discharge of the Uruguay river (Paso de los Libres station, at 29° 43' 16,90" S - 57° 04' 56,90" W) and of three tributaries of the Paraná River were analyzed (see Fig. 1A for locations of gauging stations): 1) Upper Paraná (Itatí station located at 27° 15' 58,50" S - 58° 14' 39,50" W), 2) Paraguay (Puerto Pilcomayo station, at 25° 25' 12,00" S - 57° 39' 02,20" W), and 3) Bermejo (El Colorado station, at 26° 20' 03,40" S - 59° 21' 44,70" W).

3.4. Oceanic Niño Index (ONI) data

The Oceanic Niño Index (ONI) values were downloaded from the Climate Prediction Center webpage of the National Oceanic and Atmospheric Administration (NOAA) (<http://www.cpc.ncep.noaa.gov/>). The index is calculated from the sea surface temperature

(SST) anomalies as the three month running average in the region Niño 3.4 (Equatorial Pacific). A warm (El Niño) event occurs when this anomaly is positive (above 0.5 °C) and a cold (La Niña) event occurs when it is negative (below -0.5 °C). The magnitude of the anomaly determines the intensity of the events. Even though there is no official ENSO strength definition, a further classification generally employed (e.g. <http://ggweather.com/enso/oni.htm>) will be used here, i.e. weak events occur when the SST anomaly is between 0.5 and 0.9 °C; moderate events between 1 and 1.4 °C; strong events between 1.5 and 1.9 °C, and very strong are those which exceed 2 °C.

4. Results and discussion

4.1. Validation of the remote sensing algorithm

In order to validate T derived from ocean color sensors, i.e. including atmospheric correction performance, we compare in situ measurements of T with simultaneous satellite-derived T. Even though a limited number of cloud-free match-ups were obtained during the cruises (11 and 4 for Aqua and Terra sensors, respectively), the sites covered a large extent of the estuary (squares in Fig. 1 A) and a considerable range of T values (20–200 FNU). For the fixed instrument, a total of 63 and 46 images of MA and MT, respectively, were processed for the 5 month period (Table 1). After applying the quality control criteria (see methods) and rejecting conditions of suspicious haze and remaining cloud contamination, 24 and 26 match-ups were finally retained for MA and MT respectively. Comparison of satellite-derived and field measurements for the cruises and fixed instrument showed a good agreement for both sensors with points well distributed along the 1:1 line (Fig. 2).

Statistical analysis gives regression slope close to 1 and low intercept of the linear regressions, except for IFR cruises match-ups with MT for which only 4 observations are available (Table 2). In general, good results are obtained when both data sets for each sensor are pooled together and consequently a sufficient number of observations are considered (N~30). In general, satellite-derived

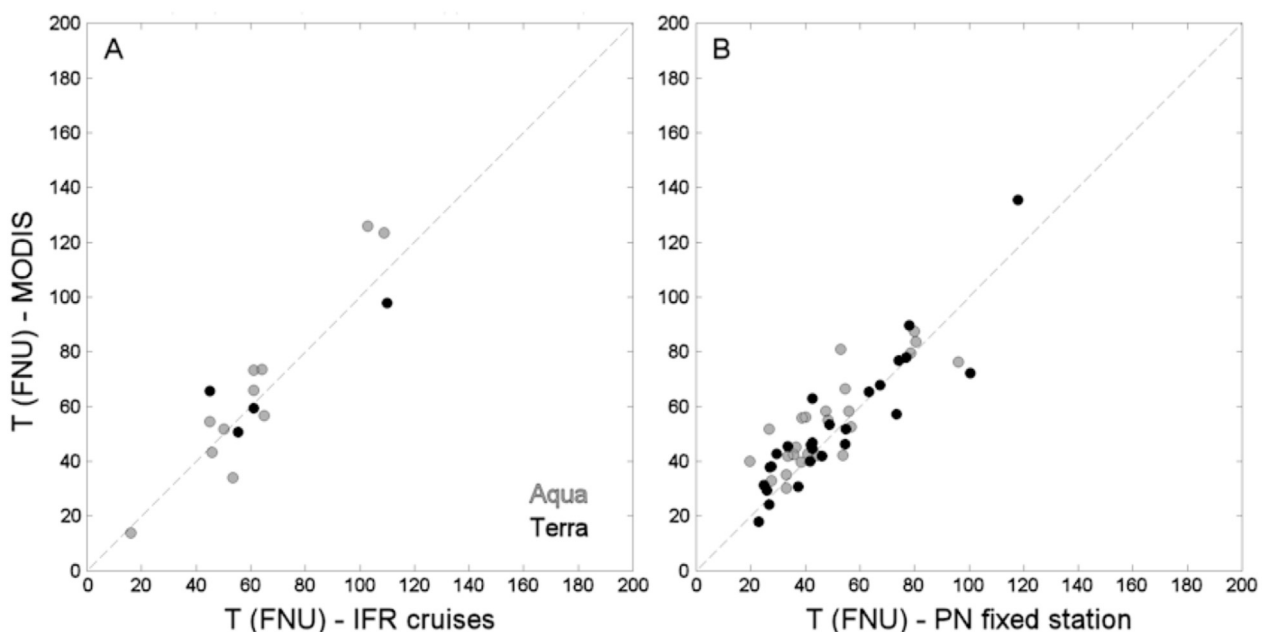


Fig. 2. Scatter plot of satellite-derived vs. measured turbidity (FNU) from: A) the samples collected during the oceanographic cruises (IFR), and B) the fixed station (PN). Match-ups for MODIS-Aqua (grey symbols) and MODIS-Terra (black symbols) are indicated. The dashed line shows the 1:1 relationship.

Table 2

Equation and statistics of the linear regressions between satellite-derived and field T [FNU] measurements for cruises (IFR) and fixed station at Pilote Norden (PN) for MODIS-Aqua and MODIS-Terra sensors. The slope, intercept, determination coefficient (R^2), root mean square (RMSE, FNU), bias (%), and mean absolute relative percentage difference (APD %) are presented for each data set, sensor (Aqua and Terra), and all data sets for each sensor. N is the number of observations.

	Slope	Intercept	R^2	RMSE	Bias ^a (%)	APD ^b (%)	N
IFR-Aqua	1.26	-12.16	0.92	7.55	3.0	15.6	11
PN-Aqua	0.73	18.8	0.69	7.80	18.7	23.9	24
All-Aqua	0.96	7.52	0.79	5.39	13.8	21.3	35
IFR-Terra	0.63	25.29	0.79	9.16	5.7	17.0	4
PN-Terra	0.91	6.62	0.83	2.93	7.0	17.3	26
All-Terra	0.87	8.58	0.83	3.64	6.9	17.3	30

$$^a \text{ bias} = \frac{1}{N} \sum \left(\frac{T^{\text{sat}} - T^{\text{in situ}}}{T^{\text{in situ}}} \right) \times 100.$$

$$^b \text{ APD} = \frac{1}{N} \sum \left(\frac{|T^{\text{sat}} - T^{\text{in situ}}|}{T^{\text{in situ}}} \right) \times 100.$$

values from both sensors slightly overestimated field data as indicated by the low but positive bias generally found (6.9% and 13.8% for MT and MA, respectively). The mean absolute relative percentage differences (APD), i.e. regardless of the sign, in the satellite-derived turbidity values are 17.3% and 21.3% for MT and MA, respectively. The slopes of the linear regressions were close to one (0.87 and 0.96 for MT and MA, respectively) and small intercept is found for both sensors (8.58 and 7.52 for MT and MA, respectively). Linear regressions explained around 80% of the variance and the root mean square errors (RMSE) were low (3.64 and 5.39 FNU for MT and MA, respectively). From these results it can be concluded that both MA and MT estimates are in good agreement with field measurements in the RdP turbid waters.

The time series of daily MA and MT retrievals were well correlated with in situ data collected at the closest time of satellite overpass at PN location ($r = 0.8$ for both MA and MT). They both reproduce the peculiar features observed in the field measurements in 2010, i.e. particularly low values all year long, specially during the months March–April when the maxima is clearly observed in 2009 and 2011, and a relative maxima in July 2010. Error bars in Fig. 3 show the spatial uncertainty of satellite data.

4.2. MODIS-Aqua and -Terra time series

To evaluate the possibility of merging both data sets, cloud-free images from MA and MT sensors collected the same day were compared; time difference between satellite passages ranged between 3 and 4 h. The relative difference between MA and MT sensors (considering their daily average) was in general about 20% varying temporally and spatially, reaching up to 100% in the highly variable regions close to the turbidity front (Barra del Indio shoal) and where the highest turbidity values are found (Punta Piedras). As an example, T maps derived from MA and MT on 25th February 2003 and the their relative difference are shown in Fig. 4.

On this day, time difference between Terra and Aqua acquisitions was ~4 hs and the highest relative difference can be observed in the region of the turbidity front (along the Barra del Indio shoal between Punta Piedras and Montevideo) and close to Punta Piedras. Also high differences can be observed in the outer estuary, seaward of the Barra del Indio shoal to the east of the surface turbidity maximum where a strong decrease of turbidity is generally observed ($T < 10$ FNU) mainly due to flocculation and deposition of sediments at the tip of the bottom salinity front (Moreira et al., 2013). Further analysis was performed between MA and MT monthly composites by extracting time series of monthly mean

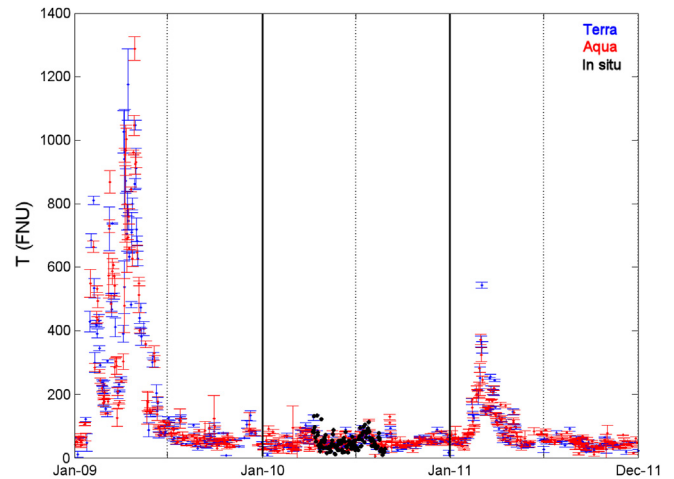


Fig. 3. Daily time series of satellite-retrieved turbidity from MODIS Terra (blue) and Aqua (red) and in situ turbidity values measured at Pilote Norden fixed station and collected at the closest time of satellite overpass (black). Error bars of the satellite data correspond to the standard deviation of the 3×3 pixel window centered at the Pilote Norden location. (For interpretation of the references to colour in this figure legend, the reader is referred to the web version of this article.)

turbidity at different sites in the upper and middle estuary. As an example, the T time series of both sensors at Pilote Norden (PN) are shown in Fig. 5. Both data sets showed the same seasonal cycle and inter-annual variability. The high frequency variability found in daily images a few hours apart is attenuated when averaging over many images per month. The differences in values between the monthly time-series that can still be observed between sensors is most likely related to differences in the time of satellite acquisition, which can be due to either the river dynamics in itself or to differences in the time of sampling of the tidal cycle. The linear relationship between MA and MT monthly mean values in the upper and middle estuary area corresponding to the 15 years had a slope of 0.99 (not shown), thus suggesting no clear bias between the sensors estimates. It is also noted that, whereas quality problems for MODIS Terra associated with calibration of blue bands are reported to affect long-term trends of oceanic chlorophyll a time series (Kwiatkowska et al., 2008), these problems do not affect estimation of turbidity and SPM from MODIS Terra using the red, near infrared and SWIR bands.

Therefore, for the time series analysis monthly averages from Terra spanning between March 2000 and July 2002 and from Aqua sensor spanning between August 2002 and December 2014 were used allowing the analysis of 15 years of consistent remotely sensing data.

4.3. Seasonal variability

To analyze the seasonal variability of RdP sediments, monthly mean turbidity maps have been calculated based on MT and MA 2000–2014 daily time series (see Data and Methods section for details). Monthly turbidity maps show clear spatial and temporal variability over the whole estuary (Fig. 6).

In the upper and middle part of the estuary, turbidity increases from January to April/May, with higher values in the southern coast (Argentina) compared to the northern coast (Uruguay), and decreases from June to September. Relatively high values all through the year can be observed in the region associated with the mean position of the maximum turbidity front along the Barra del Indio shoal and a persistent maximum throughout the year can be clearly observed in Punta Piedras, a region highly correlated with an area

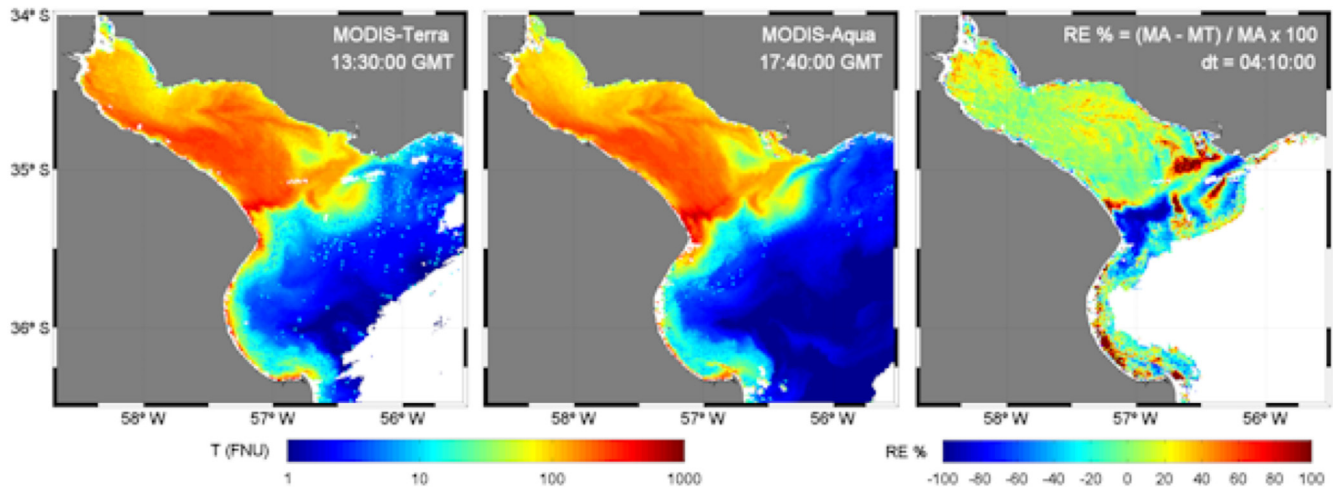


Fig. 4. Daily turbidity image of 25 February 2003 derived from MODIS Terra (left) and Aqua (center), and the relative percentage difference image between Aqua and Terra (right). In the latter, pixels with $T < 5$ FNU are masked because of the noise-related detection limit.

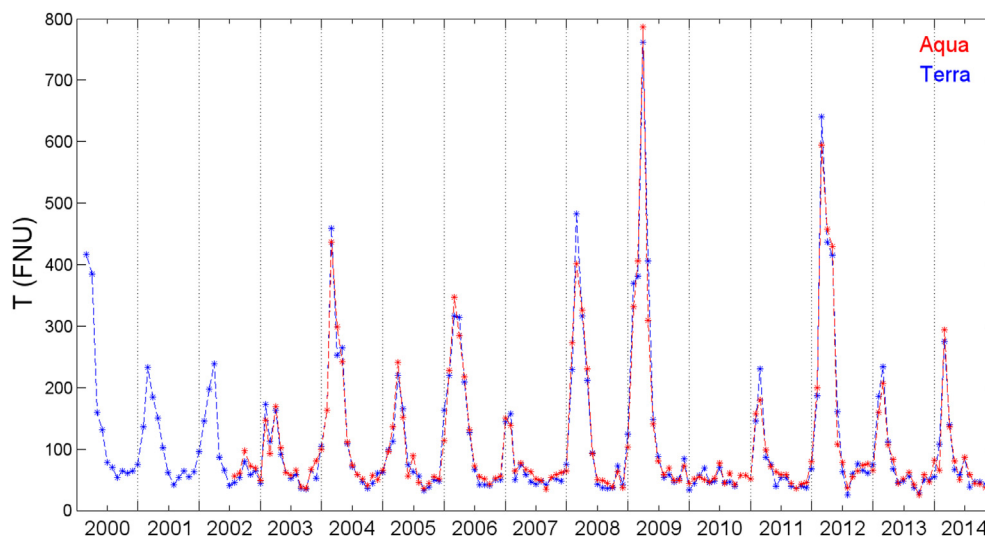


Fig. 5. Monthly time series of turbidity from MODIS-Terra (blue) and MODIS-Aqua (red) at Pilote Norden (see location in Fig. 1B). (For interpretation of the references to colour in this figure legend, the reader is referred to the web version of this article.)

of maximum tidal currents and dissipation by bottom friction (Simionato et al., 2004a). In order to clarify the spatial variability and its relation to the seasonality, the month when the maximum and minimum turbidity value is more frequent and the percentage of occurrence was estimated for each pixel during the 2000–2014 period (Fig. 7).

The spatial distribution of the month when the turbidity maximum and minimum are most frequent shows a clear pattern along the axis of the estuary. In the upper and upper-middle estuary the turbidity maximum occurs most frequently in March (50–60% of years considered), in the lower-middle estuary it occurs in April–May (40–50%), while it is highly variable in the outer region of the estuary (Fig. 7A and C). Finally, in the Samborombón bay the maximum occurs in November. It's worth noting that the outer region and Samborombón bay show the lowest observed frequency (20–30%). In turn, the minimum value is most frequently observed in August–September in the upper estuary, in October in most of the middle estuary with peaks in July along the southeast margin, in January in the turbidity front area, and in May–June–July in Samborombón bay (Fig. 7B). This spatial distribution in the upper

and middle estuary suggests that the timing of the maximum and minimum value could be related to the RdP discharge. To better illustrate the seasonality in different regions and its relation to the mean river outflow, the mean annual cycle was extracted from six sites located in the upper estuary (UE), northern margin (NM), southern margin (SM), Punta Piedras (PP), and two sites along the Barra del Indio shoal (Bla and B1b). The median value of 11×11 pixel window centered at each site and the mean RdP outflow are plotted in Fig. 8.

The monthly mean variations in general show a marked seasonal cycle in all sites, but less pronounced in the northern part of the Barra del Indio shoal close to the Uruguayan margin (B1b Fig. 7). In general, T values increased from January to May with maxima in March–April and minima in September–October. It should be noted that along the Argentine coast close to Punta Piedras turbidities were much higher and the month of occurrence of the main peak was highly variable (Fig. 7A and C) as seen also in Fig. 6. As mentioned before, along the Uruguayan coast (NM and B1b) T values are much lower and their seasonal fluctuations have smaller amplitude than along the Argentine coast (e.g. SM and PP). This

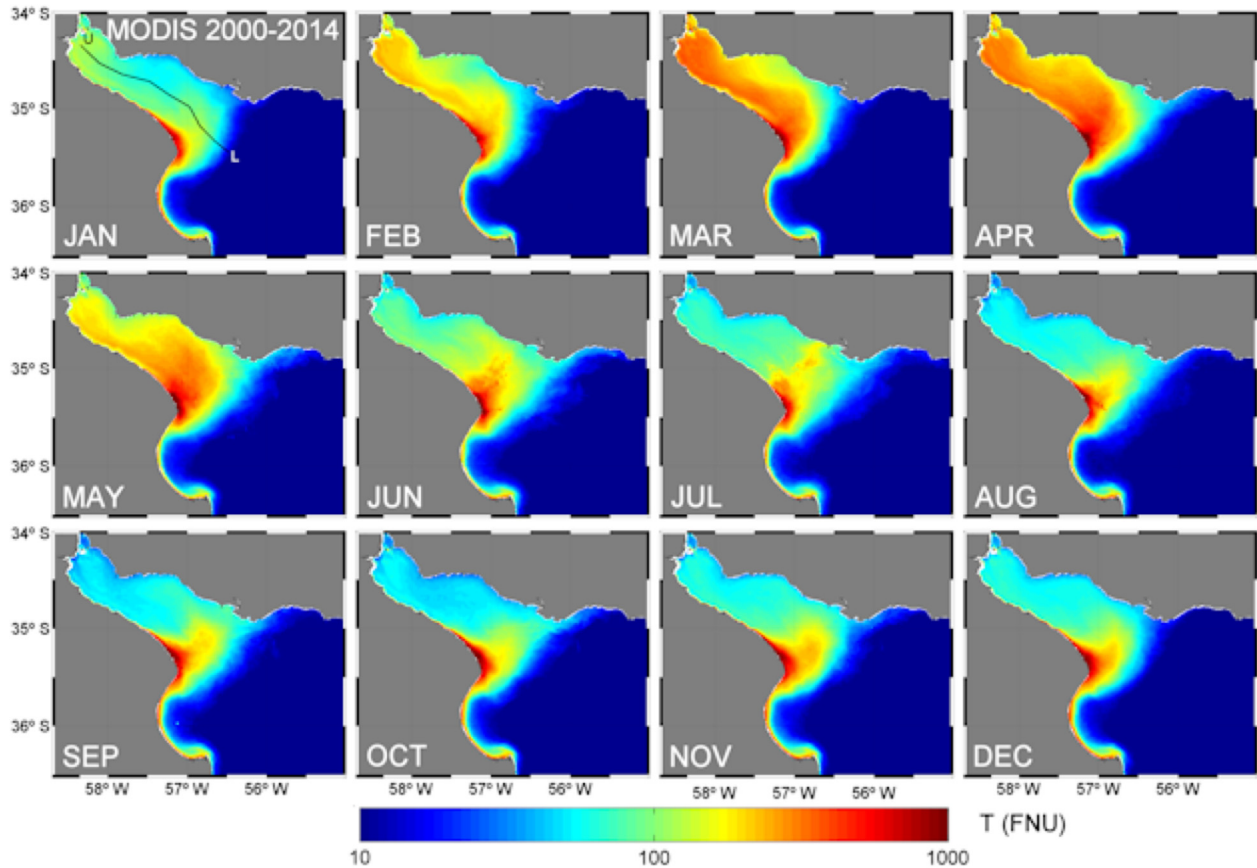


Fig. 6. Multi-annual monthly mean turbidity maps for the 2000–2014 period using MODIS-Terra (Mar 2000–Jul 2002) and MODIS-Aqua (Aug 2002–Dec 2014) data. The along-estuary section UL, used to present results later in Fig. 12, is shown in the top left image.

asymmetrical spatial distribution of the sediments is in agreement with previous works (López Laborde and Nagy, 1999; Moreira et al., 2013). Moreira et al. (2013) relate this differential pattern to the fact that most of the solid discharge comes from the Paraná River (which flows along the southern coast) compared to the Uruguay River (which flows along the northern coast), and that stronger tidal currents occur along the southern coast of the estuary inducing more re-suspension of sediments and thus higher concentration of suspended matter. The RdP outflow presents weak seasonal variability with relative maxima in May and October–November (Fig. 8). Statistically significant correlation coefficients between the RdP mean runoff and the T long-term monthly mean values at UE ($r = 0.51$), NM ($r = 0.81$), SM ($r = 0.7$), PP ($r = 0.51$), Bla ($r = 0.72$) and Blb ($r = 0.68$) have been found (Fig. 8). Thus, the RdP runoff seems to partially account for the seasonal variability of turbidity in different parts of the estuary. However, the large standard deviations around the monthly means (from 70% to 100% of the mean discharge) suggests high inter-annual variations as will be analyzed later. Therefore, further analysis was performed here regarding the water discharge of different tributaries of RdP.

Time series of monthly T at Pilote Norden (PN) in the upper RdP (see Fig. 1B for locations) and percentage of water discharge respect to the total RdP water discharge of four tributaries of RdP are presented in Fig. 9 (see Fig. 1A for locations of gauging stations). The plots show no clear correlation between time series of turbidity and any of the Uruguay (% Q_U), Upper Paraná (% Q_{UP}) or Paraguay (% Q_P) rivers' percentage runoff, while the seasonal variability of turbidity does closely match the percentage water discharge variations of the

Bermejo River (% Q_B) (Table 3).

The highest solid discharges supplied by the Upper Bermejo basin coincide with peak Bermejo liquid discharge, reaching the annual maximum during the rainy season in February–March (Cotta, 1963). In turn, the T time series at the upper RdP peaks in March–April, around a month after the Bermejo highest water discharge (Fig. 9). A statistically significant cross-correlation (highest peak) between Bermejo outflow and the 15 years monthly T time-series at PN (0.62) was found with a positive lag at 1 month, thus increasing the correlation coefficient from 0.72 to 0.8 when a one-month lag is considered (Table 3). This time difference of one month is in agreement with previous mean estimates of the sediment travel time (Simionato et al., 2009; Moreira et al., 2013). However, the amplitude of the T time series at PN does not seem to correlate with the amplitude of Bermejo river water discharge, the mean annual discharge of which is just ~2% of total RdP runoff (~450 m³ s⁻¹). This inter-annual variability of peak T in the RdP will be further analyzed in section 4.4.

The turbidity mean seasonal pattern described in the present study is not completely in accordance with what was previously found by Moreira et al. (2013) also using remote sensing data. That paper analyzed 10 years of MODIS-Aqua data (2002–2012) of total suspended matter using the OC5 algorithm (Gohin et al., 2005; Gohin, 2011) and found that in the upper and middle estuary the suspended matter concentration increases in the austral fall (March–May) which was related with the Bermejo water discharge, but reached a peak in austral winter (June–August), decreasing to minimum values in austral summer (December–February). The discrepancy between these and our results is

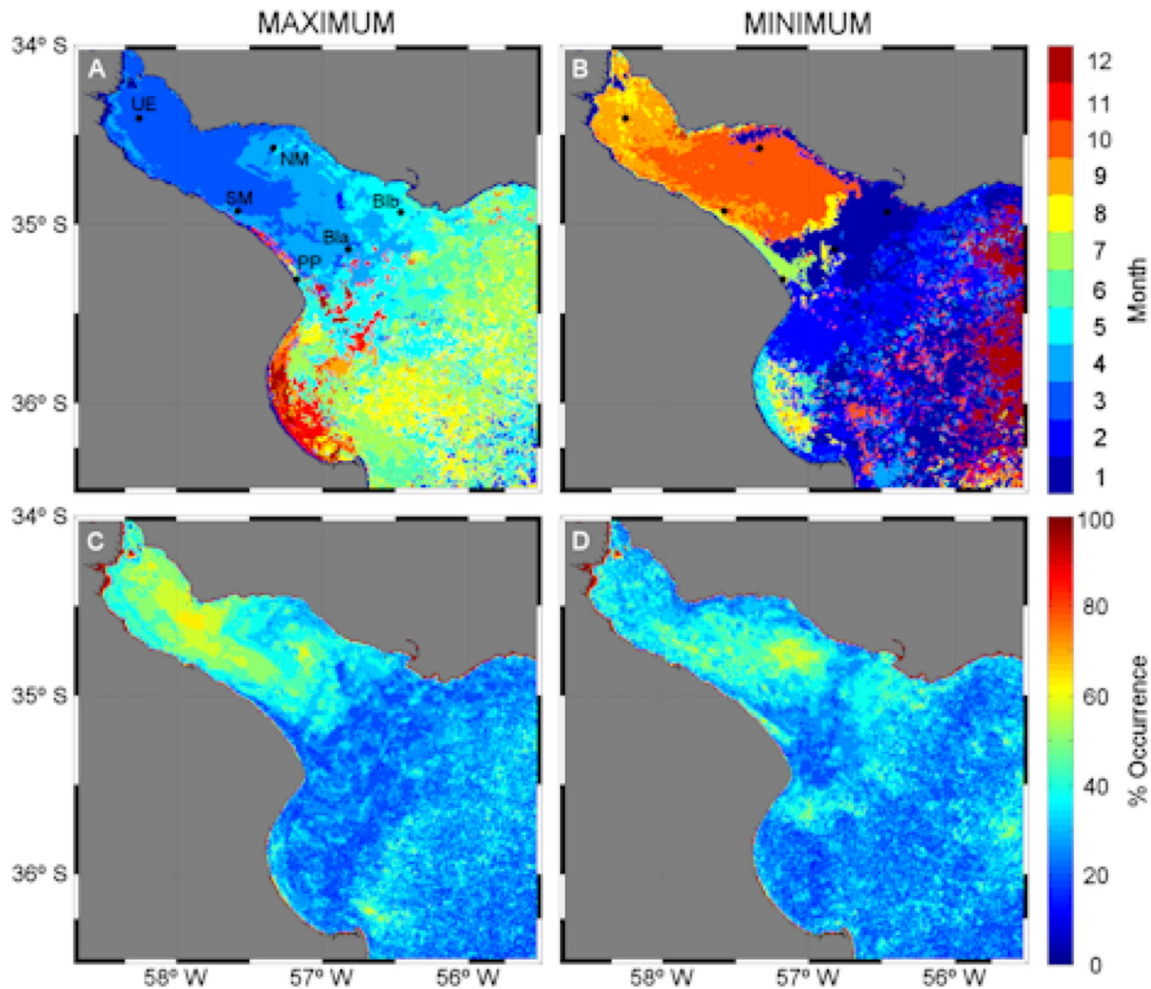


Fig. 7. Spatial distribution of the month when the maximum (A) and minimum (B) turbidity is most frequently observed based on monthly turbidity maps from MODIS-Aqua and Terra images for the period 2000–2014. Spatial distribution of the percentage of occurrence of maximum (C) and minimum (D) for the corresponding month. In the upper left figure the locations of points used for subsequent time series analysis are denoted: Upper Estuary (UE), Northern Margin (NM), Southern Margin (SM), Punta Piedras (PP), and Barra del Indio (Bla and Blb) sites.

most likely related to differences in the processing of the satellite data. [Moreira et al. \(2013\)](#) used standard level 2 reflectance data, which were processed using the NASA standard atmospheric correction algorithm ([Stumpf et al., 2003](#); [Bailey et al., 2010](#)). It has been previously shown that the standard atmospheric correction completely fails to retrieve water reflectance in most of the Rdp turbid waters mainly due to sensor saturation of the bands 667, 748 and 869 nm used for the atmospheric correction and the incorrect estimation of the marine contribution in the near infrared in these extremely turbid waters ([Dogliotti et al., 2011](#)). Thus, the highest values of suspended matter were probably missing from their analysis due to failure of the atmospheric correction procedure. Moreover, the authors removed values higher than 98 g m^{-3} thus excluding the highest values which are known to occur and which have been previously measured in this region ([Urien, 1966, 1967](#); [C.A.R.P., 1989](#); [Dogliotti et al., 2014, 2015](#)). Actually, the match-up analysis performed in [Moreira et al. \(2013, their Fig. 3a\)](#), showed a clear underestimation of field measurements at high concentrations. Moreover, a more detailed match-up analysis using the same database showed a poor performance of the OC5 algorithm in this region ([Camiolo et al., 2016](#)). The time series of continuous in situ turbidity measurements measured in Pilote Norden and used in both the [Moreira et al. \(2013\)](#) and the present study was collected

between April and August 2010 and showed relatively high T values in April and July. The satellite-derived time series used in the present study shows that 2010 was an exceptional year with relatively low T values observed all year long and the expected maximum in April–May, clearly observed in 2009 and 2011 and in most of the years, is not present in 2010 ([Fig. 3](#)). This is related to the effect of a moderate El Niño event that took place that year, as described in the next section.

4.4. Inter-annual variability

To describe the inter-annual variability of turbidity in the Rdp, time series of monthly T at selected sites (PN, NM, and SM, see [Figs. 1A and 7A](#)), annual turbidity anomaly maps, and a space-time plot of monthly T along a section are analyzed. The section runs from $58^{\circ}30' \text{ W}$ at the upper region of the estuary through $56^{\circ}30' \text{ W}$ well outside the turbidity plume, running through the middle of the river (UL section indicated in [Fig. 6 - JAN](#)).

The T time series at the three selected sites located in different parts of the upper and middle estuary reveal strong inter-annual variability with largest amplitude in 2009 and 2012 and smallest amplitudes in 2003, 2007 and 2010 ([Fig. 10](#)). The lowest T amplitudes are related to high Rdp outflow in 2003 and 2007

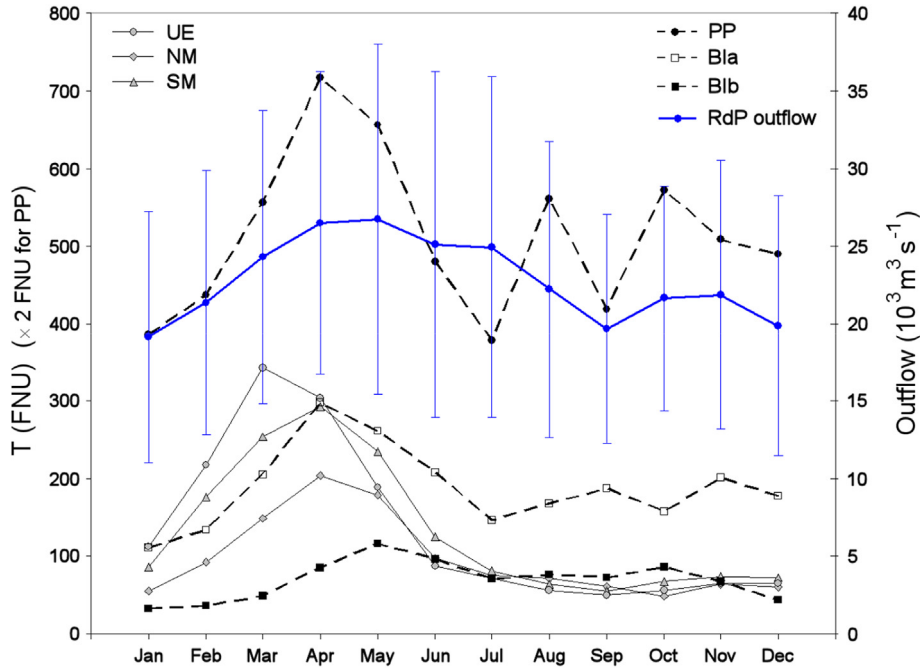


Fig. 8. Monthly mean time-series (average over 2000–2014) of RdP mean outflow (Borús and Giacosa, 2014) and standard deviation (blue line and bars), and turbidity (black) at the Upper Estuary (UE), Northern Margin (NM), Southern Margin (SM), Punta Piedras (PP), and Barra del Indio (Bla and Blb) sites (see location in Fig. 7). (For interpretation of the references to colour in this figure legend, the reader is referred to the web version of this article.)

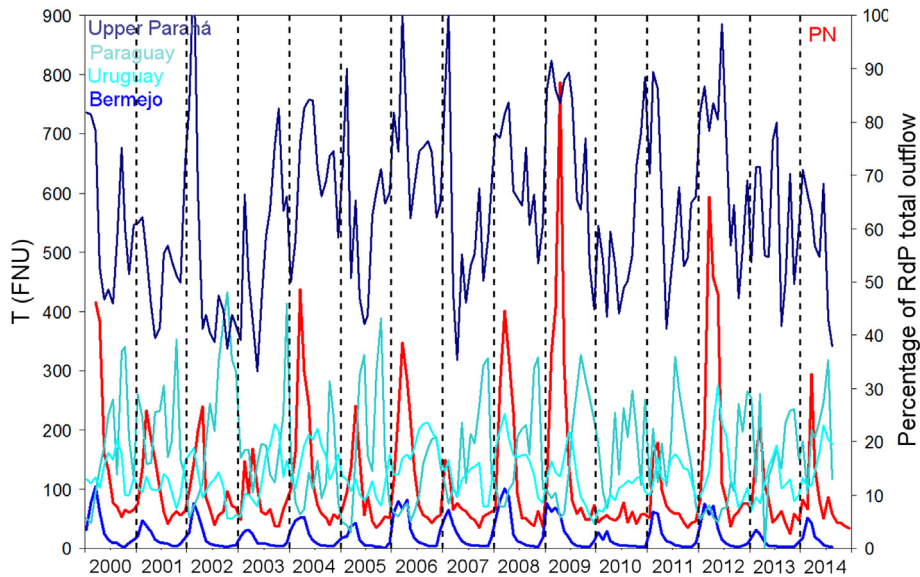


Fig. 9. Satellite-derived turbidity time series at PN (red) and monthly percentage of RdP total outflow water discharge of Upper Paraná (Itatí), Paraguay (Pto. Pilcomayo), Uruguay (Paso de los Libres), and Bermejo (El Colorado) rivers (Subsecretaría de Recursos Hídricos). (For interpretation of the references to colour in this figure legend, the reader is referred to the web version of this article.)

Table 3

Pearson correlation coefficient (r) between the percentage of the water discharged by the each of the tributaries considered ($\%Q_i$) respect to the RdP total water discharge ($\%Q_i = Q_i/Q_{RdP} \times 100$) and T time-series at PN. UP: Upper Paraná, PA: Paraguay, U: Uruguay, B: Bermejo, and RdP: Río de la Plata. All correlations are statistically significant at 99%, and * at 95%.

	$\%Q_{UP}$	$\%Q_{PA}$	$\%Q_U$	$\%Q_B$ (lag=1month)
r	0.36	0.22*	-0.40	0.72 (0.80)

($\sim 40,000 \text{ m}^3 \text{ s}^{-1}$) and 2010 ($\sim 50,000 \text{ m}^3 \text{ s}^{-1}$), when the outflow was about twice the mean outflow ($22,500 \text{ m}^3 \text{ s}^{-1}$). In turn, the largest T amplitudes were related to low RdP outflow in 2000 ($12,000 \text{ m}^3 \text{ s}^{-1}$), 2004 ($12,900 \text{ m}^3 \text{ s}^{-1}$), 2008 ($15,000 \text{ m}^3 \text{ s}^{-1}$), 2009 ($11,500 \text{ m}^3 \text{ s}^{-1}$) and 2012 ($13,800 \text{ m}^3 \text{ s}^{-1}$).

Annual turbidity anomalies show the strong inter-annual variability previously observed and confirm that its spatial distribution is similar in the upper and middle estuary, but show an inverse pattern around the Barra del Indio region in all of the years except in 2000, 2003, 2012 and 2013 (Fig. 11). In turn, in the outer estuary

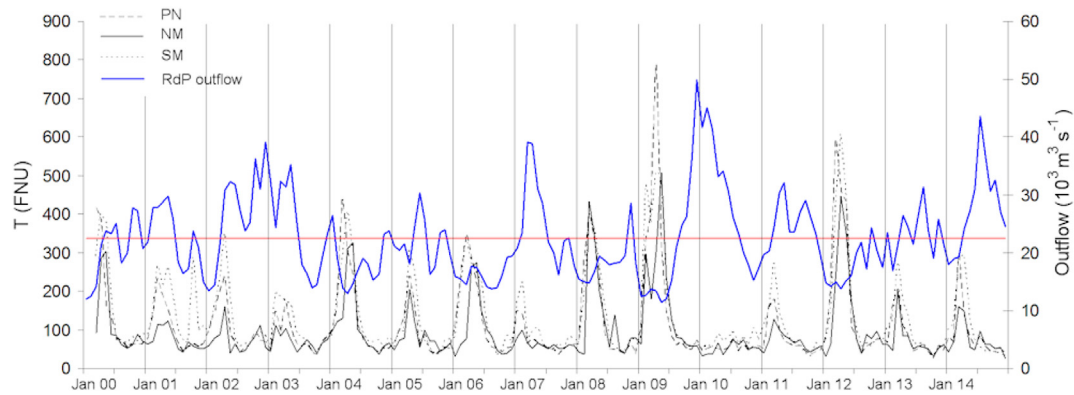


Fig. 10. Monthly time series (2000–2014) of T (FNU - black) at PN (dashed), NM (solid) and SM (dotted) and RdP outflow ($10^3 \text{ m}^3 \text{ s}^{-1}$) (blue). Mean river outflow ($22,500 \text{ m}^3 \text{ s}^{-1}$) is indicated (red an) (Borús and Giacosa, 2014). (For interpretation of the references to colour in this figure legend, the reader is referred to the web version of this article.)

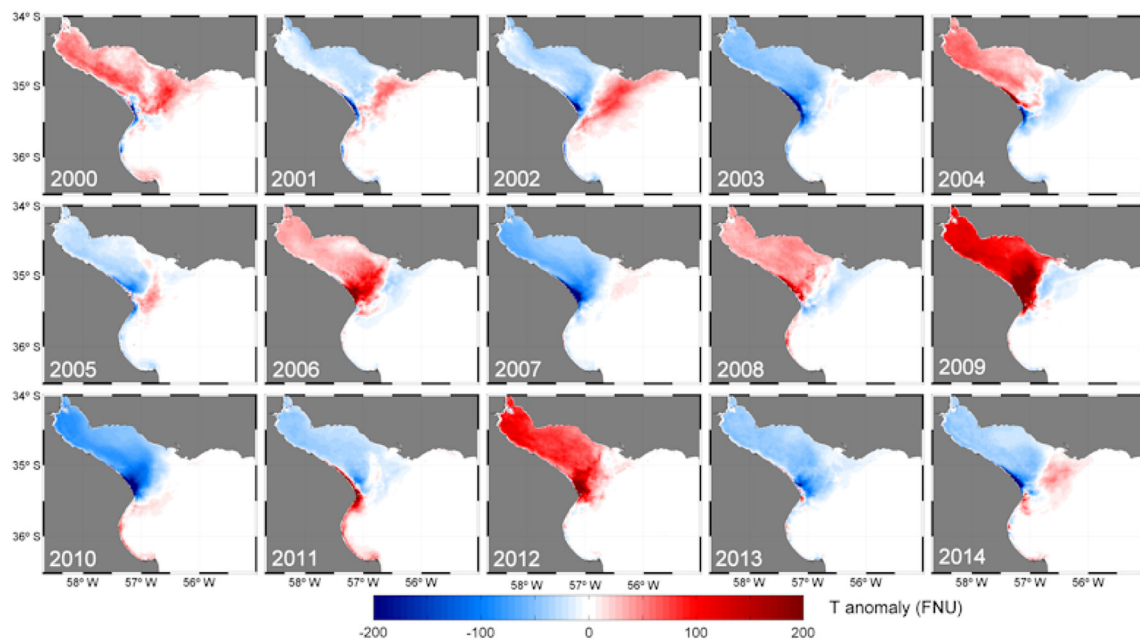


Fig. 11. Annual anomaly turbidity maps illustrating the inter-annual variability.

the variability was much lower, except in 2002 (along the Uruguay coast) and in 2010 and 2011 (along the Samborombón coast) when positive anomalies were observed. In the upper and middle estuary, positive anomalies can be observed in 2000, 2006, 2008, 2009 and 2012, being strongest in 2009 and 2012 (>150 FNU). In turn, negative anomalies can be observed in 2001, 2002, 2003, 2005, 2007, 2010, 2011, 2013 and 2014 with minimum values in 2003, 2007 and 2010 (<-100 FNU). The inverse pattern of the T anomalies in the frontal region seems to be related to the influence of the magnitude of the river outflow on the extension of the river plume. As a response to larger river outflow (negative T anomaly in the upper/middle estuary) the plume extension increases resulting in positive T anomalies around Barra del Indio given that sediments reach farther. In turn, when the river outflow is low (positive T anomaly in the upper/middle estuary) a retraction in the river plume is expected resulting in negative T anomalies around Barra del Indio. It should be noted that these are annual anomalies that show a general pattern, i.e. this inverted pattern which are clearly observed in monthly anomaly maps (not shown) are attenuated by averaging in the annual maps, and that the extension of the plume

is not only determined by the river outflow, but also by the wind stress (Piola et al., 2008).

Turbidity, RdP outflow anomaly and the Oceanic Niño Index (ONI) along the section UL are presented in Fig. 12. As seen previously in Fig. 6, along the upper and middle estuary (from $58^{\circ}30'$ to $57^{\circ}W$) the well-defined seasonal pattern of high turbidity from February to May can be observed in most of the years, while more variable turbidity and a less clear seasonality is observed in the outer region east of $57^{\circ}W$ (Fig. 12 left panel). Moreover, the inter-annual variability of peak turbidity is clearly observed and seems to be related to the RdP outflow anomaly and in turn with the ENSO cycle (Fig. 12 right panel). Large RdP outflow in 2003, 2007 and 2010, when turbidity was low, occur during moderate and weak El Niño events in the corresponding years (Fig. 12). In turn, higher turbidity can be observed in years where RdP outflow mean values were lower than the mean and are related with weak and moderate La Niña events in 2000, 2008, 2009, and 2012 (Fig. 12). As an exception, the high turbidity observed in 2004 associated to low RdP outflow ($12,900 \text{ m}^3 \text{ s}^{-1}$) is not related to a La Niña event.

Eastern South America is particularly subject to ENSO-triggered

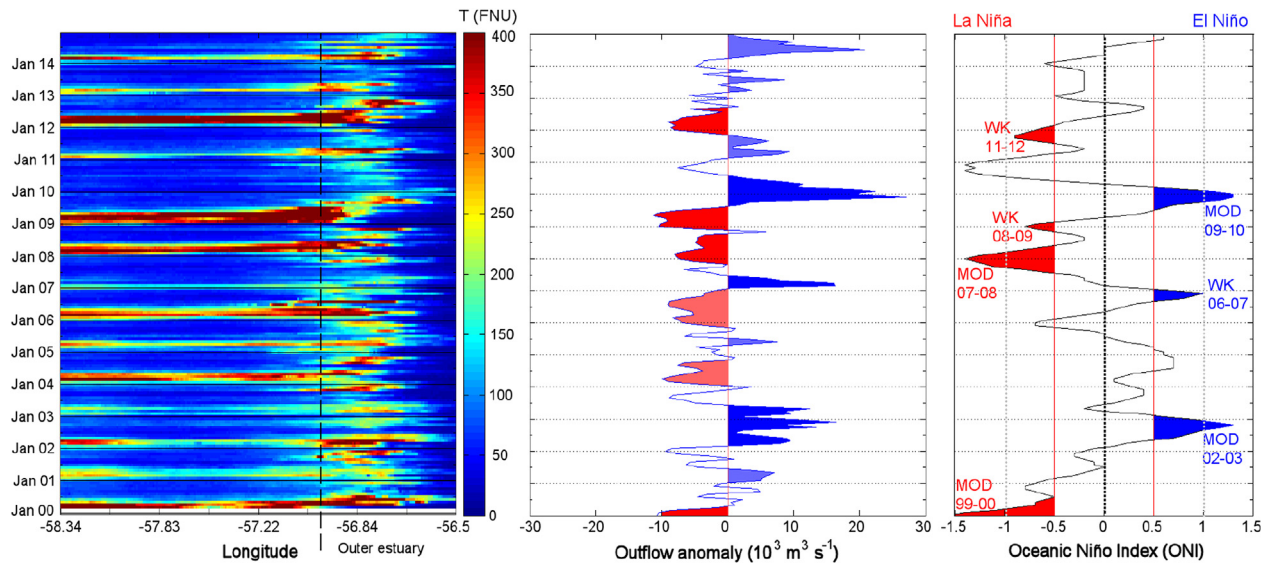


Fig. 12. left) Space-time plot of T (FNU) along section UL for the period 2000–2014 (see Fig. 6 for location); center) monthly RdP outflow anomaly ($10^3 \text{ m}^3 \text{ s}^{-1}$) (Borús and Giacosa, 2014). Positive (negative) outflow anomaly related with high T values are shown in blue (red); right) Oceanic Niño Index 3-month running average values. Weak (WK) and moderate (MOD) El Niño (La Niña) events related to positive (negative) outflow anomaly are shown in light-blue (pink). (For interpretation of the references to colour in this figure legend, the reader is referred to the web version of this article.)

floods. It has been shown that the two main components of the La Plata basin, the Paraná and Uruguay rivers, show a strong inter-annual oscillation in phase with El Niño events (Pasquini and Depetris, 2007), with increased water discharge during ENSO warm events (El Niño) and normal to low discharges during cold events (La Niña). However, the Bermejo and Pilcomayo Rivers are exceptions and do not show this periodicity (Pasquini and Depetris, 2007). Therefore, the inter-annual pattern found in this work can be explained by the fact that the Bermejo river that contributes with most of the sediments (~70%) is not affected by the ENSO cycle, while the main tributaries that provide more than 97% of the RdP liquid discharge (Paraná and Uruguay rivers) are highly influenced by the increased rains during El Niño events. This produces an increase in the water discharging to the Atlantic Ocean through the RdP, but not in the amount of sediments, which are mainly provided by the Bermejo River, thus producing a dilution effect in the RdP during El Niño events (Figs. 3 and 10). This is confirmed by the strong correlation found between the percentage of the water discharged by the Bermejo river respect to the RdP total water discharge ($\%Q_B$), which can be considered as an index of the solid respect to the liquid discharge of RdP, and the T time-series at PN with a correlation coefficient $r = 0.72$ and 0.8 when no lag and a 1-month lag were considered respectively (Table 2). In turn, higher amplitude in the turbidity seasonal cycle can be observed in years when RdP water discharge is lower than average and is more pronounced in some years associated with La Niña events, like 2000, 2007, 2008, and 2011 (Figs. 11 and 12). However, the relation between increases in turbidity and La Niña events is not so direct as that for the El Niño events because La Niña events are not the only predictor for drought in this region (Mechoso and Pérez Iribarren, 1992).

5. Conclusions

The results presented in this study show the usefulness of a long time series of reliable satellite-derived data to study spatio-temporal variability and long term change of turbidity in the RdP provided that remote sensing algorithms suitable for extremely turbid waters are chosen, e.g. a SWIR based atmospheric correction

(Wang and Shi, 2007) and a turbidity retrieval algorithm which switches to near infrared wavelengths in the most turbid waters (Dogliotti et al., 2015). Turbidity retrievals with uncertainties of 21 and 17% from MODIS Aqua and MODIS Terra data, were found. Based on a long time series of quality controlled data, the seasonal dynamics of the RdP showed that, in the upper and middle river, variations of turbidity are highly correlated with the Bermejo river runoff, with maxima in March–April (around a month after the peak Bermejo liquid and solid discharge) and minima in August–September. This seasonality does not completely agree with previous findings (Moreira et al., 2013), but this difference is probably related to the use of inappropriate remote sensing algorithms (which are known to fail in highly turbid waters) in the previous work. Additional long-term field measurements are needed in this region to confirm the findings in the present study.

At a longer time scale, high inter-annual variability in turbidity has been observed and related to the ENSO cycle. Low amplitude and turbidity values have been observed in El Niño years and high amplitude and turbidity values during some La Niña years. This pattern is explained here by the different responses of the tributaries to this inter-decadal event. While the solid flux, essentially from the Bermejo river, is not significantly affected by the ENSO cycle, the water discharge from the other tributaries is significantly affected, giving a consequent dilution of turbidity and SPM concentration.

Other studies using long time series of satellite derived SPM data have shown that the variability of sediment input is mainly controlled by the river discharge (Loisel et al., 2014; Petus et al., 2014). However, the peculiar characteristics of the La Plata basin, which covers almost the whole width of the continent, draining tributaries with very different characteristics that respond to different hydrologic regimes, showed a more complex relation between SPM and the water discharge of the main and tributary rivers as well as their response to climatic forcing such as the ENSO cycle. Given that SPM is the variable of main interest in sediment transport studies, future work will aim at deriving SPM maps from satellite-derived turbidity by finding local relations between these variables. To achieve this, field measurements of both SPM and T at different places and time of year are essential to assess its spatial and

temporal variability.

The results presented here highlight the utility of long time series of remote sensing data in assessing and monitoring changes of key environmental parameters and in understanding sediment transport dynamics. The current methodology may be of use in understanding the spatial, seasonal and interannual variability of turbidity and suspended particulate matter in other estuaries and river plumes.

Acknowledgements

The authors thank the DAAC (NASA) for providing MODIS satellite data. The research was supported by the FFEM (Fonds Français pour l'Environnement Mondial of France) in the frame of the PNUD/GEF RLA/99/G31 FREPLATA Project, the BELSPO (Belgian Federal Science Policy Office) contracts BELCOLOUR-ARG and TURBINET (BL/58/FWI10), the ANPCyT (National Agency for Scientific and Technological Research of Argentina) PICT 2014-0455, and the CONICET (National Council for Scientific and Technological Research of Argentina) PIP 112 20120100350 Projects. The three anonymous reviewers are thanked for their useful comments.

References

- Aceituno, P., 1988. On the functioning of the Southern oscillation in the south American sector. Part I: surface climate. *Mon. Weather Rev.* 116, 505–524.
- Bailey, S.W., Franz, B.A., Werdell, P.J., 2010. Updated NIR water-leaving radiance estimation for ocean color data processing. *Opt. Express* 18, 7521–7527.
- Berri, G.S., Ghietto, M.A., Garcia, N.O., 2002. The influence of ENSO in the flows of the Upper Parana River of South America over the past 100 years. *J. Hydrometeorol.* 3, 57–65.
- Borús, J., Giacosa, J., 2014. Evaluación de caudales diarios descargados por los grandes ríos del sistema del plata al río de la plata. Dirección de Sistemas de Información y Alerta Hidrológico Instituto Nacional del Agua, Ezeiza, Argentina, 2014.
- Boschi, E.E., 1988. El ecosistema estuarial del Río de la Plata (Argentina y Uruguay). *An. Inst. Cienc. Mar Limnol. Univ. Nac. Autónoma México* 15 (2), 159–182.
- Boss, E., Taylor, L., Gilbert, S., Gundersen, K., Hawley, N., Janzen, C., Johengen, T., Purcell, H., Robertson, C., Schar, D.W.H., Smith, G.J., Tamburri, M.N., 2009. Comparison of inherent optical properties as a surrogate for particulate matter concentration in coastal waters: optical properties as proxies of particulate matter. *Limnol. Oceanogr. Methods* 7 (11), 803–810.
- Brea, J.D., Spalletti, P., 2010. Generación y transporte de sedimentos en la Cuenca Binacional del Río Bermejo. Caracterización y análisis de los procesos intervinientes. COBINABE, Buenos Aires.
- Camilloni, I.A., Barros, V.R., 2003. Extreme discharge events in the Parana River and their climate forcing. *J. Hydrol.* 278, 94–106.
- Camiolo, M., Cozzolino, E., Simionato, C.G., Hozbor, M.C., Lasta, C.A., 2016. Evaluating the performance of the OC5 algorithm of IFREMER for the highly turbid waters of Río de la Plata. *Braz. J. Oceanogr.* 64 (1), 19–28.
- C.A.R.P., 1989. Estudio para la evaluación de la contaminación en el Río de la Plata. Comisión Administradora del Río de la Plata, Montevideo, Buenos Aires, 422 pp.
- Cotta, R., 1963. Influencia sobre el Río Parana del material sólido transportado por el Río Bermejo (Influence on the River Parana of the solid material transported by the River Bermejo). Comisión Nacional del Río Bermejo. Publ. no. 92 EH.
- Depetris, P.J., Griffins, J.J., 1968. Suspended load in the Río de la Plata drainage basin. *Sedimentology* 11, 53–60.
- Depetris, P.J., Kempe, S., Latif, M., Mook, W.G., 1996. ENSO-controlled flooding in the Parana River (1904–1991). *Naturwissenschaften* 83, 127–129.
- Devlin, M., Schaffelke, B., 2009. Spatial extent of riverine flood plumes and exposure of marine ecosystems in the Tully coastal region, Great Barrier Reef. *Mar. Freshw. Res.* 60, 1109–1122.
- Diaz, A.F., Studzinski, C.D., Mechoso, C.R., 1998. Relationships between precipitation anomalies in Uruguay and southern Brazil and sea surface temperatures in the Pacific and Atlantic Oceans. *J. Clim.* 11, 251–271.
- Dogliotti, A.I., Ruddick, K.G., Nechad, B., Doxaran, D., Knaeps, E., 2015. A single algorithm be used to retrieve turbidity from remotely-sensed data in all coastal and estuarine waters. *Remote Sens. Environ.* 156, 157–168. <http://dx.doi.org/10.1016/j.rse.2014.09.020>.
- Dogliotti, A.I., Ruddick, K., Nechad, B., Lasta, C., 2011. Improving Water Reflectance Retrieval from MODIS Imagery in the Highly Turbid Waters of La Plata River. In: Proceedings of VI International Conference "Current Problems in Optics of Natural Waters" St. Petersburg, Russia. Publishing House "Nauka" of RAS.
- Dogliotti, A.I., Camiolo, M., Simionato, C., Jaureguizar, A., Guerrero, R., Lasta, C., 2014. First optical observations in the turbidity maximum zone in the Río de la Plata estuary: a challenge for atmospheric correction algorithms. In: Proceeding of Ocean Optics XXII Conference. Portland (ME), United States of America.
- Drago, E.C., Amsler, M.L., 1988. Suspended sediment at a cross section of the middle Paraná river: concentration, granulometry and influence of the main tributaries. In: Bordas, P., Walling, D.E. (Eds.), *Sediment Budgets*. IAHS, Wallingford, UK, 38 1–396.
- Fabricius, K.E., Logan, M., Weeks, S.J., Lewis, S.E., Brodie, J., 2016. Changes in water clarity in response to river discharges on the Great Barrier Reef continental shelf: 2002–2013. *Estuar. Coast. Shelf Sci.* 173, A1–A15.
- Falcini, N., Khan, S., Macelloni, L., Horton, B.P., McKee, K.L., Santoleri, R., Colella, S., Li, C., Lutken, C.B., Volpe, G., D'Emidio, M., Salusti, A., Jerolmack, D.J., 2012. Linking the historic 2011 Mississippi River flood to coastal wetland sedimentation. *Nat. Geosci.* 5 (11), 803–807.
- Frañan, M., Brown, O., 1996. Study of the Río de la Plata turbidity front, Part 1: spatial and temporal distribution. *Cont. Shelf Res.* 16, 1259–1282. [http://dx.doi.org/10.1016/0278-343\(95\)00071-2](http://dx.doi.org/10.1016/0278-343(95)00071-2).
- García, N.O., Mechoso, C.R., 2005. Variability in the discharge of South American rivers and in climate. *Hydrol. Sci. J.* 50, 459–477.
- Gohin, F., Loyer, S., Lunven, M., Labry, C., Froidefond, J.M., Delmas, D., Huret, M., Herbland, A., 2005. Satellite-derived parameters for biological modelling in coastal waters: illustration over the eastern continental shelf of the Bay of Biscay. *Remote Sens. Environ.* 95, 29–46.
- Gohin, F., 2011. Annual cycles of chlorophyll-a, non-algal suspended particulate matter, and turbidity observed from space and in-situ in coastal waters. *Ocean Sci.* 7, 705–732.
- Guerrero, R.A., Acha, E.M., Frañan, M.B., Lasta, C.A., 1997. Physical oceanography of the Río de la Plata Estuary, Argentina. *Cont. Shelf Res.* 17 (7), 727–742.
- Guerrero, R.A., Piola, A., Molinari, G., Osiroff, A., 2010. Climatología de temperatura y salinidad en el Río de la Plata y su Frente Marítimo, Argentina-Uruguay. Instituto Nacional de Investigación y desarrollo Pesquero INIDEP, Mar del Plata, 95 pp.
- Kwiatkowska, E.J., Franz, B.A., Meister, G., McClain, C.R., Xiong, X., 2008. Cross calibration of ocean-color bands from moderate resolution imaging spectroradiometer on Terra platform. *Appl. Opt.* 47 (36), 6796–6810.
- Loisel, H., Mangin, A., Vantrepotte, V., Dessailly, D., Garnesson, P., Ouilon, S., Lefebvre, J.-P., Mériaux, X., Ngoc Dinh, D., Minh Phan, T., 2014. Variability of suspended particulate matter concentration in coastal waters under the Mekong's influence from ocean color (MERIS) remote sensing over the last decade. *Remote Sens. Environ.* 150, 218–230.
- López Laborde, J., Nagy, G.J., 1999. Hydrography and sediment transport characteristics of the Río de la Plata: a review. In: Perillo, G.M.E., Piccolo, M.C., Pino, M. (Eds.), *Estuaries of South America: Their Geomorphology and Dynamics*. Springer, pp. 133–160.
- Meccia, V.L., Simionato, C.G., Fiore, M.M.E., D'Onofrio, E., Dragani, W., 2009. Sea surface height variability in the Río de la Plata estuary from synoptic to inter-annual scales: results of numerical simulations. *Estuar. Coast. Shelf Sci.* 85, 327–343.
- Mechoso, C., Pérez Iribarren, G., 1992. Streamflow in southeastern South America and the southern oscillation. *J. Clim.* 5, 1535–1539.
- Miller, R.L., Twardowski, M., Moore, C., Casagrande, C., 2003. 03. The Dolphin: technology to support remote sensing bio-optical algorithm development and applications. *Backscatter* 14 (2), 8–12.
- Moreira, D., Simionato, C.G., Gohin, F., Cayocca, F., Clara Tejedor, M.L., 2013. Suspended matter mean distribution and seasonal cycle in the Río de La Plata estuary and the adjacent shelf from ocean color satellite (MODIS) and in-situ observations. *Cont. Shelf Res.* 68, 51–66.
- Pasquini, A.I., Depetris, P.J., 2007. ENSO-triggered exceptional flooding in the Paraná River: where is the excess water coming from? *J. Hydrol.* 383 (2010), 186–193.
- Pedrozo, F., Bonetto, C., 1987. Nitrogen and phosphorus transport in the Bermejo river (South America). *Rev. Hydrobiol. Trop.* 20, 91–99.
- Petus, C., Marieu, V., Novoa, S., Chust, G., Bruneau, N., Froidefond, J.M., 2014. Monitoring spatio-temporal variability of the Adour River turbid plume (Bay of Biscay, France) with MODIS 250-m imagery. *Cont. Shelf Res.* 74, 35–49.
- Piola, A., Romero, S., Zajaczkovski, U., 2008. Space–time variability of the Plata plume inferred from ocean color. *Cont. Shelf Res.* 28, 1556–1567.
- Robertson, A.W., Mechoso, C.R., 1998. Interannual and decadal cycles in river flows of Southeastern South America. *J. Clim.* 11, 2570–2581.
- Robertson, A.W., Mechoso, C.R., Garcia, N.O., 2001. Interannual prediction of the Parana river. *Geophys. Res. Lett.* 28, 4235–4238.
- Ropelewski, C.H., Halpert, S., 1987. Global and regional scale precipitation patterns associated with the El Niño/Southern Oscillation. *Mon. Weather Rev.* 115, 1606–1626.
- Ropelewski, C.H., Halpert, S., 1989. Precipitation patterns associated with the high index phase of the Southern Oscillation. *J. Clim.* 2, 268–284.
- Sarubbi, A., 2007. Análisis del avance del Frente del Delta del Río Paraná. Tesis de Ingeniería Civil. Facultad de Ingeniería, Universidad de Buenos Aires, 145 pp.
- Schroeder, T., Devlin, M.J., Brando, V.E., Dekker, A.G., Clementson, L.A., McKinna, L., 2012. Inter-annual variability of wet season freshwater plume extent into the Great Barrier Reef lagoon based on satellite coastal ocean colour observations. *Mar. Pollut. Bull.* 65, 210–223.
- Simionato, C.G., Dragani, W.C., Nuñez, M.N., Engel, M., 2004a. A set of 3-D nested models for tidal propagation from the Argentinean Continental Shelf to the Río de la Plata estuary: Part I. *M. J. Coast. Res.* 20 (3), 893–912.
- Simionato, C.G., Dragani, W., Meccia, V., Nuñez, M., 2004b. A numerical study of the barotropic circulation of the Río de la Plata estuary: sensitivity to bathymetry, earth's rotation and low frequency wind variability. *Estuar. Coast. Shelf Sci.* 61 (2), 261–273.

- Simionato, C.G., Meccia, V., Dragani, W., Guerrero, R., Nuñez, M., 2006. The Rio de la Plata estuary response to wind variability in synoptic to intra-seasonal scales: barotropic response. *J. Geophys. Res. C Oceans* 111, C09031. <http://dx.doi.org/10.1029/2005JC003297>.
- Simionato, C.G., Meccia, V., Guerrero, R., Dragani, W., Nuñez, M., 2007. The Rio de la Plata estuary response to wind variability in synoptic to intra-seasonal scales: II currents vertical structure and its implications on the salt wedge structure. *J. Geophys. Res. C Oceans* 112, C07005. <http://dx.doi.org/10.1029/2006JC003815>.
- Simionato, C.G., Meccia, V.L., Dragani, W.C., 2009. On the path of plumes of the Río de la Plata estuary main tributaries and their mixing time scales. *Geoscientia* 34, 87–116.
- Simionato, C.G., Tejedor, M.L.C., Campetella, C., Guerrero, R., Moreira, D., 2010. Patterns of sea surface temperature variability on seasonal to sub-annual scales at and offshore the Rio de la Plata Estuary. *Cont. Shelf Res.* 30, 1983–1997.
- Simionato, C.G., Moreira, D., Re, M., Fossati, M., 2011. Estudio de la dinámica hidrosedimentológica del Río de la Plata: observación y modelación numérica de los sedimentos finos, 109 pp.. Published by Proyecto FREPLATA, CTMFCARP. ISBN 978-92-990052-9-3.
- Stumpf, R.P., Arnone, R.A., Gould Jr., R.W., Martinolich, P.M., Ransibrahmanakul, V., 2003. A Partially Coupled Ocean-atmosphere Model for Retrieval of Water-leaving Radiance from Seawifs in Coastal Waters. NASA Tech. Memo. 206892. National Aeronautics and Space Administration, Goddard Space Flight Center, Greenbelt, MD.
- Syvitski, J.P.M., 2003. Supply and flux of sediment along hydrological pathways: research for the 21st century. *Glob. Planet. Change* 39, 1–11.
- Tossini, L., 1959. Sistema hidrográfico cuenca del Río de la Plata. *An. la Soc. Científica Argent.* 167 (3–4), 41–64.
- UNESCO, 2007. World Water Assessment Programme, La Plata Basin Case Study Final Report. unesdoc.unesco.org/images/0015/001512/151252e.pdf.
- Urien, C.M., 1966. Distribución de los sedimentos modernos de1 Río de la Plata superior. *Publ. H-106. Serv. Hidrogr. Nav. Armada Argent.* 3 (3), 197–203.
- Urien, C.M., 1967. Los sedimentos modernos de1 Río de la Plata Exterior. *Publ. H-106. Serv. Hidrogr. Nav. Armada Argent.* 4 (2), 113–213.
- Walling, D.E., Webb, B.W., 1996. Erosion and sediment yield: a global overview. In: Walling, D.E., Webb, B.W. (Eds.), *Erosion and Sediment Yield: Global and Regional Perspectives*. (Proc. Exeter Symposium, July, 1996), IAHS Publication No. 236. IAHS Press, Wallingford, UK, pp. 3–19.
- Wang, M., 2007. Remote sensing of the ocean contributions from ultraviolet to nearinfrared using the shortwave infrared bands: simulations. *Appl. Opt.* 46, 1535–1547.
- Wang, M., Shi, W., 2007. The NIR-SWIR combined atmospheric correction approach for MODIS ocean color data processing. *Opt. Express* 15 (24), 15722–15733. <http://dx.doi.org/10.1364/OE.15.015722>.